



ORIGINAL RESEARCH ARTICLE

# Formation of Ultrafine Graphite Nodules in Ductile Iron and its Effects on Mechanical Properties

Chen Liu, Yuzhou Du , Pengchun Li, Xin Wang, Wanting Sun, Caiyin You, and Bailing Jiang

Submitted: 27 May 2023 / Revised: 25 July 2023 / Accepted: 3 August 2023

The evolution of ductile iron with martensitic matrix during annealing at 700 °C was studied in the present study. The results showed that the ultrafine graphite nodules with a count of 8500 nod/mm<sup>2</sup> and an average diameter of about 1 μm were obtained in ductile iron through annealing treatment. The martensite in ductile iron was first decomposed into granular cementite, and then, the granular cementite aggregated and gradually transformed into ultrafine graphite nodules. With the annealing time extended to 90 min, the martensite was completely transformed into ferrite and ultrafine graphite nodules. These results implied that martensite in ductile iron was a good starting microstructure for forming the high graphite nodules in ductile iron by solid phase transition. The precipitation of ultrafine graphite nodules improved strength and plasticity of ductile iron, which was mainly because ultrafine graphite nodules refined ferrite grains, weakened stress concentration, and hindered crack propagation during deformation. The present study provided a new method to increase graphite nodule count in ductile iron.

**Keywords** annealing, cementite, ductile iron, martensite, ultrafine graphite nodules

## 1. Introduction

Cast iron is first found in 500 BC (Ref 1), which is still most used in modern industry. The morphology of graphite in cast iron could be flake (in gray cast iron), intermediate (in compacted or vermicular cast iron), or spheroidal (in nodular or ductile cast iron) (Ref 2-4), which determines its mechanical response (Ref 5). The morphology of graphite in cast iron can be tailored to be spheroid by adding small amounts of Mg in Fe-Si-C melts during solidification (Ref 6), which attenuates the detrimental effects of graphite on mechanical properties (Ref 7). Therefore, nodular cast iron with a good combination of strength and toughness is widely used in various structural applications including automotive, mining and railway (Ref 8-10).

It should be emphasized that the count, homogeneity, and nodularity of graphite in ductile iron affect the physical and mechanical properties (Ref 11-13), in which graphite nodule count is considered to be the critical factor (Ref 14). The graphite nodule count in ductile iron is mainly determined by cooling rate, spheroidization and inoculation methods (Ref 15). For instance, a thin-walled ductile iron casting with a thickness less than 3 mm contained the graphite nodule count more than

2000 nod/mm<sup>2</sup> because of the high cooling rate during solidification (Ref 16); an ultrafine ductile iron castings with the graphite nodule count exceeding 3000 nod/mm<sup>2</sup> was obtained via strictly controlling magnesium treatment (Ref 17). It should be noted that such high cooling rate is only suitable to produce ductile iron with thin-wall, and magnesium treatment is complex and immature.

Previous investigations attempted to introduce graphite in white cast iron or free cutting steels to increase their wear resistance by solid phase transformation (Ref 18-22). For instance, the graphitic white iron was developed for abrasive wear application to enhance thermal and wear properties (Ref 23, 24); a dispersed graphite in medium carbon steel with high Si and Al contents (Si > 1.8% and Al > 1.3%) was observed by a solid-state annealing process (Ref 18, 25-27). The addition of graphitizing elements, such as Al and Si, is required for the formation of graphite in steels or cast iron via solid phase transformation (Ref 28). However, the graphite is difficult to produce in white iron by graphitization treatment due to low silicon content (< 1%), which requires graphitization at high temperatures for long time (Ref 29, 30). Additionally, the formation of graphite is very sensitive to the initial microstructure during heat treatment (Ref 31). For example, graphite particles nucleation in ferrite-pearlite starting microstructure is located in the pearlite regions (Ref 19); graphite particles nucleation in bainite starting microstructure is evident at bainitic ferrite plate boundaries and the size of graphite forming in bainite is smaller than that in ferrite-pearlite (Ref 26, 27). It was found that graphite could be easily formed in medium carbon steel with the martensite matrix (Ref 19, 26).

Compared with white cast iron and medium carbon steel, ductile iron contains large amounts of Si (Si > 2%) and C (C > 3%) elements (Ref 32), which provides composition prerequisite for the precipitation of graphite during solid phase transformation. Additionally, carbon atoms can be dissolved from spheroidal graphite into austenite through austenization treatment (Ref 33, 34). Hence, referring to the principle of

Chen Liu, Yuzhou Du, Pengchun Li, Xin Wang, Caiyin You, and Bailing Jiang, School of Materials Science and Engineering, Xi'an University of Technology, Xi'an 710048, People's Republic of China; and Wanting Sun, Department of Electrical Engineering, University of Nebraska-Lincoln, 1400 R St, Lincoln, NE 68588. Contact e-mail: duyuzhou@xaut.edu.cn.

graphitization in medium carbon steel, it is inferred that the graphite can be obtained in ductile iron. Therefore, a ductile iron with martensite matrix was annealed treatment to investigate the precipitation process of graphite, in the objective to provide novelty methods of tailoring graphite nodule count in ductile iron.

## 2. Materials and Experimental

A cylindrical ductile iron casting with a diameter of 30 mm was fabricated via a horizontal continuous casting, as described previously (Ref 35) in detail. The chemical composite of as-cast ductile iron used in the present study was 3.52 wt.%C, 2.45 wt.%Si,  $Mn \leq 0.1$  wt.%, 0.015 wt.% S, 0.022 wt.%P, 0.049 wt.%Mg, 0.011 wt.%RE, and balanced Fe, which was analyzed using a spark optical emission spectrometer. Two strips with dimensions of 10 mm  $\times$  20 mm  $\times$  100 mm were cut from the cast profiles, and then, one strip was heated to 900 °C and held for 90 min in a vertical furnace. After that, the sample quenched into oil to obtain a martensitic matrix. The other of strip was heated to 900 °C and held for 90 min, and then, the strip was cooled in furnace to room temperature in order to obtain traditional ferrite ductile iron as a comparison group. The quenched specimen was machined into the dimensions of 10 mm  $\times$  10 mm  $\times$  10 mm. Annealing of the samples was made at 700 °C from 0 to 90 min.

Characterization of microstructural evolution during annealing process was performed by OLYMPUS GX71 optical microscope (OM), and JSM-6700F scanning electron microscopy (SEM) with an accelerating voltage of 30 kV after being ground, polished and etched by 4% nital solution. Besides, extensive SEM work was carried out on specimens deep etched by 20% nital solution for 40 min to reveal the evolution of spheroidal graphite. XRD was carried out on an XRD-7000

diffractometer with a scanning angle from 35 to 85° and the scanning speed was 4°/min. The samples were analyzed using (EDS) to qualitatively characterize microzonal composition. The working voltage of SEM imaging and EDS was 10 kV.

Ferritic ductile iron with ultrafine graphite nodule (FDI-Gr) was obtained by quenching and then annealing at 700 °C for 90 min. Ferritic ductile iron without ultrafine graphite nodule (FDI) was obtained by annealing at 900 °C for 90 min and then cooled in furnace. Tensile tests were carried out at room temperature using a universal testing machine (HT-2402) with a crosshead speed of 1 mm/min on these two samples to compare its mechanical properties. Sample cross sections were obtained with an area of 4  $\times$  2 mm<sup>2</sup> and a gauge length of 21 mm. For each specimen, at least three samples were used to ensure repeatability. The stress distribution was simulated by the commercial software ABAQUS during tensile testing, which was to further assist to explain the mechanical properties differences of the two samples. The parameters for the simulation were as follows. Young's modulus of ferrite matrix was 19 GPa, and Poisson's ratio was 0.27. During the loading process, the left end of the model was fixed and a tension load of 200 MPa was applied to the right side, with a true strain of 1%.

## 3. Results

### 3.1 The Precipitation of Ultrafine Graphite Nodule from Martensite in Ductile Iron

Figure 1 presents the optical images of the as-quenched sample annealed for different times. A typical microstructure containing high carbon acicular martensite (Fig. 1a) could be observed for the as-quenched sample. After annealing for 5 min, a small amount of white irregular ferrite appeared around the graphite nodule (Fig. 1b). With the increase in

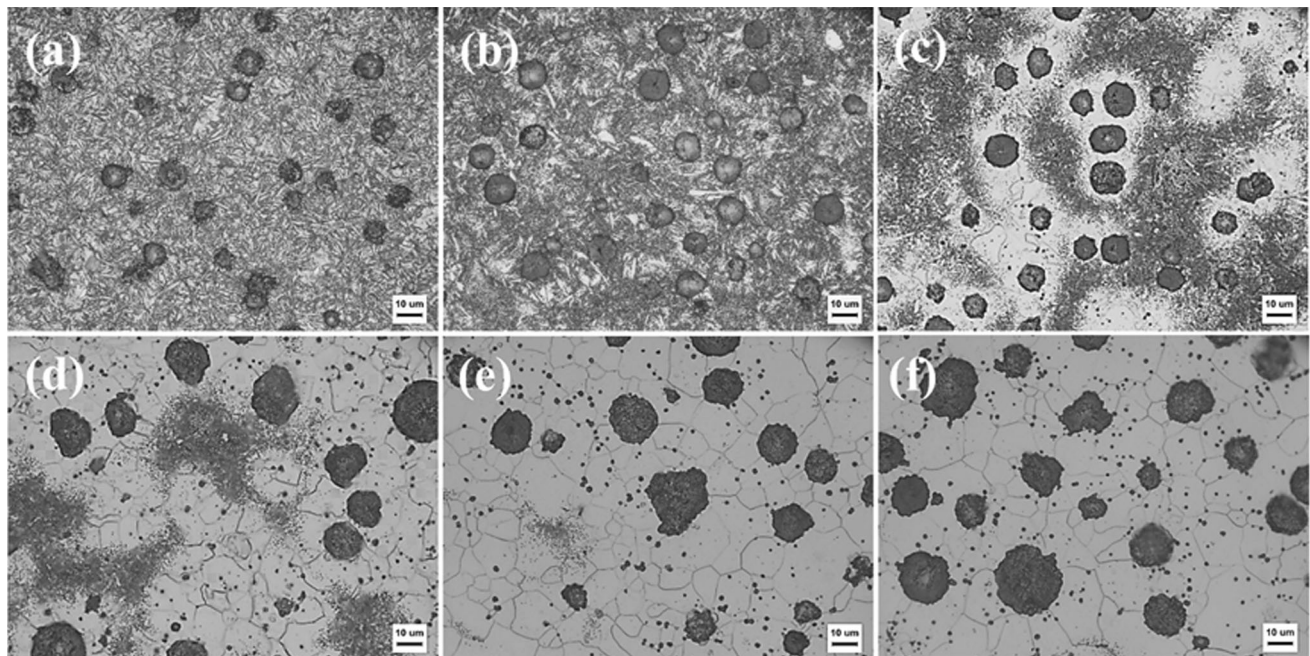


**Fig. 1** Optical images of as-quenched ductile iron annealed at 700 °C for (a) 0 min, (b) 5 min, (c) 10 min, (d) 20 min, (e) 60 min and (f) 90 min

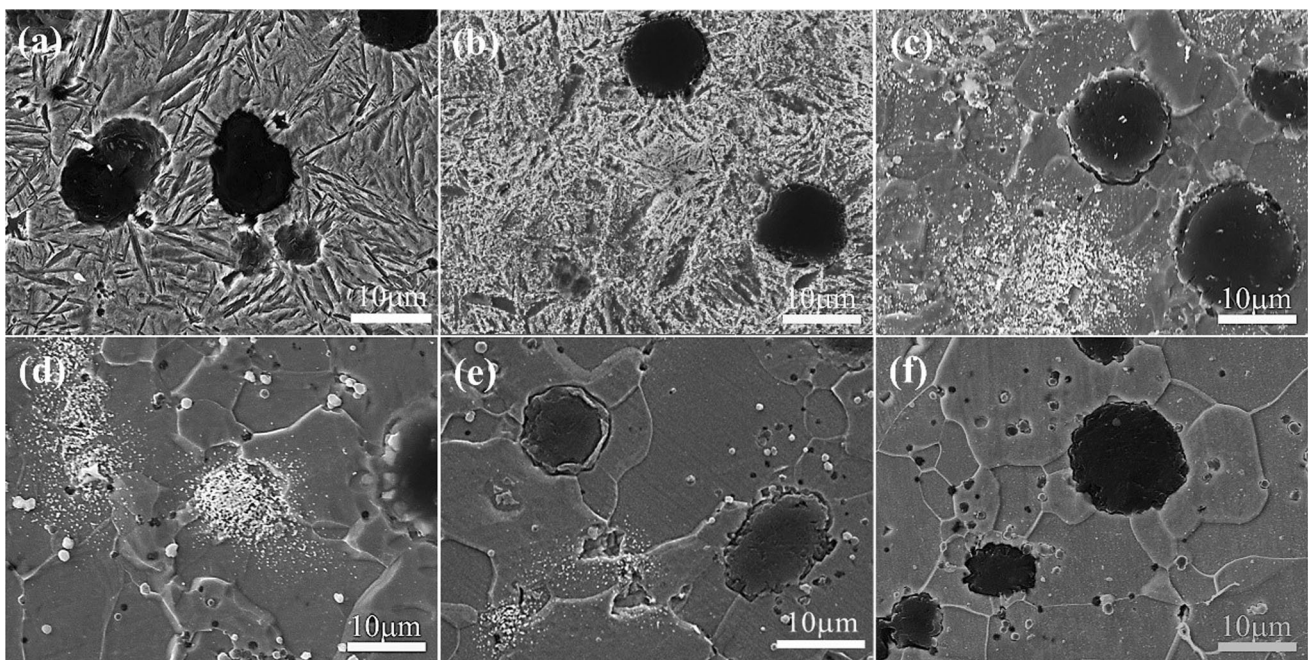
annealing time, martensite was decreased (Fig. 1b–d), and only a small amount of martensite could be detected for sample annealed for 20 min (Fig. 1d). It should be noted that some ultrafine graphite nodules appeared in ferrite region. Interestingly, the martensite in the vicinity of spheroidal graphite was directly transformed into ferrite, but the acicular martensite far away from the spheroidal graphite was transformed into carbide particles and ferrite. After annealing 60 min, only tiny graphite nodule, initial spheroidal graphite and ferrite existed in the samples (Fig. 1e). Further prolonging the annealing time (Fig. 1f), the number of tiny graphite nodule was increased. The diameter of ultrafine graphite nodule was estimated about 1  $\mu\text{m}$ , which was much smaller than the initial spheroidal graphite ( $\sim 25 \mu\text{m}$ ).

Figure 2 shows the SEM images of the as-quenched sample annealing for different times. It could be seen that the as-quenched ductile iron was mainly composed of acicular martensite and retained austenite (Fig. 2a). After 5 min annealing (Fig. 2b), the acicular martensite decomposed and was hardly to be recognized. It is known that martensite would rapidly decompose into cementite and ferrite during high temperature tempering (Ref 36) because high carbon martensite was metastable. After 10 min annealing (Fig. 2c), a large amount of ferrite appeared around the initial spheroidal graphite, but carbide particles were mainly distributed far from initial graphite nodular. This microstructural characteristic was varied with that in conventional steels (Ref 18). Additionally, small amounts of tiny graphite were detected in ferrite. With further prolonging the annealing time to 20 min (Fig. 2d), martensite was totally disappeared and the tiny graphite particles and a few carbides distributed around ferrite. Cementite could hardly be detected when the sample was annealed for 60 min (Fig. 2e), and the microstructure of ductile iron was composed of ferrite, initial spheroidal graphite, and ultrafine graphite nodules, which indicated that cementite was transformed into graphite. The count of tiny graphite nodule was increased when the annealing time increased to 90 min and the

cementite almost completely disappeared, which implied that the graphitization process was almost completed (Fig. 2f).

Figure 3 presents the variation of volume fraction of ferrite and count of ultrafine graphite nodules with annealing time. The volume fraction of ferrite and number of ultrafine graphite nodules both increased with the increase in annealing time, which indicated that the formation of ferrite was closely related to the precipitation of graphite. The ferrite and graphite began to form after annealing for 10 min. After 90 min annealing, the martensitic matrix was completely transformed into ferrite, and the ultrafine spheroidal graphite with a count of 8500 nod/ $\text{mm}^2$  was obtained. The graphite parameters in martensite ductile iron after annealing 90 min are summarized in Table 1. The size of precipitated graphite nodules was small, only about 1  $\mu\text{m}$ . Thus, the nodularity of precipitated ultrafine graphite nodules cannot be accurately evaluated. Besides, it could be seen that the nodule count of ultrafine graphite nodules was very high compared with that of the initial spheroidal graphite in ductile iron after annealing for 90 min. The average diameter and average nearest-neighbor distance of ultrafine graphite nodule were very small compared to the initial spheroidal graphite in ductile iron.

Figure 4 presents XRD patterns of the quenched samples annealing for different times. The diffraction peaks of  $\alpha$  phase were detected for all samples (Fig. 4a), which corresponded to martensite or ferrite. It should be noted that the diffraction peak of  $\text{Fe}_3\text{C}$  was detected for sample after annealing for 5 min, which indicated that the supersaturated carbon in martensite precipitated in the form of carbide during initial annealing. When the annealing time was further prolonged to 10, 20, 60 and 90 min, the diffraction peak of  $\text{Fe}_3\text{C}$  disappeared. It indicated that  $\text{Fe}_3\text{C}$  decreased or even completely decomposed. From the magnified image (Fig. 4b), it could be seen that the (110) diffraction peaks of  $\alpha$  phase shifted to high angle, indicating that the saturation of solid solution carbon atoms in  $\alpha$  phase decreased.



**Fig. 2** SEM images of as-quenched ductile iron annealed at 700 °C for (a) 0 min, (b) 5 min, (c) 10 min, (d) 20 min, (e) 60 min and (f) 90 min

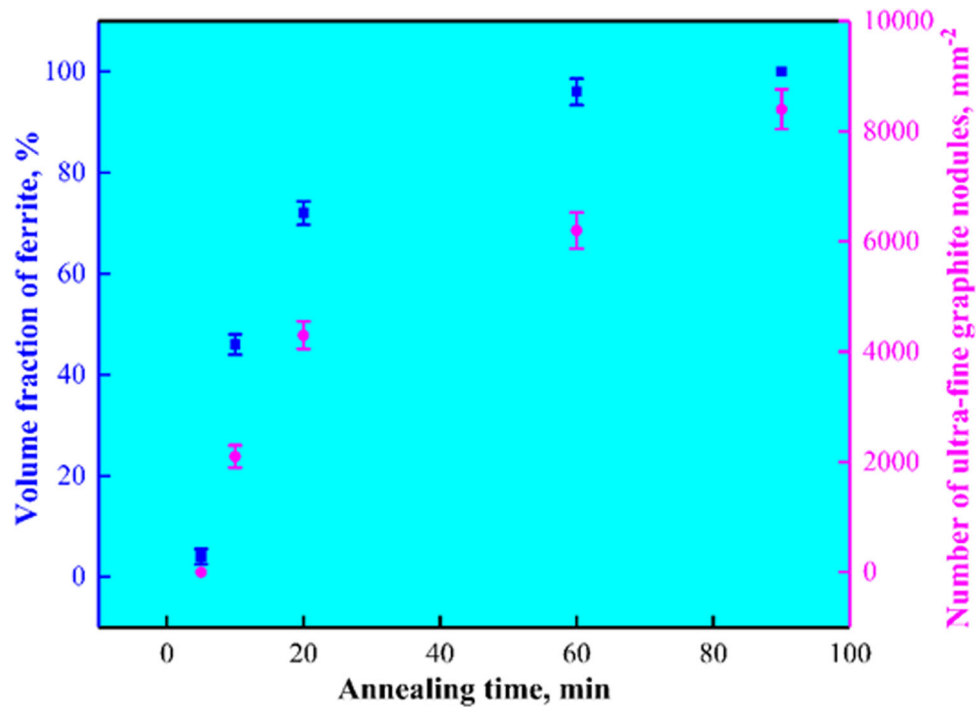


Fig. 3 Variation of volume fraction of ferrite and ultrafine graphite nodules count with annealing time

Table 1 Results of graphite parameters in martensite ductile iron after annealing 90 min

Graphite	Nodule count, nod/mm <sup>2</sup>	Average diameter, $\mu\text{m}$	Nodularity, %	Average nearest-neighbor distance, $\mu\text{m}$
Initial spheroidal graphite	$310 \pm 20$	$18 \pm 1$	85	$17 \pm 2$
Ultrafine graphite nodule	$8500 \pm 360$	$1 \pm 0.3$	...	$2 \pm 0.6$

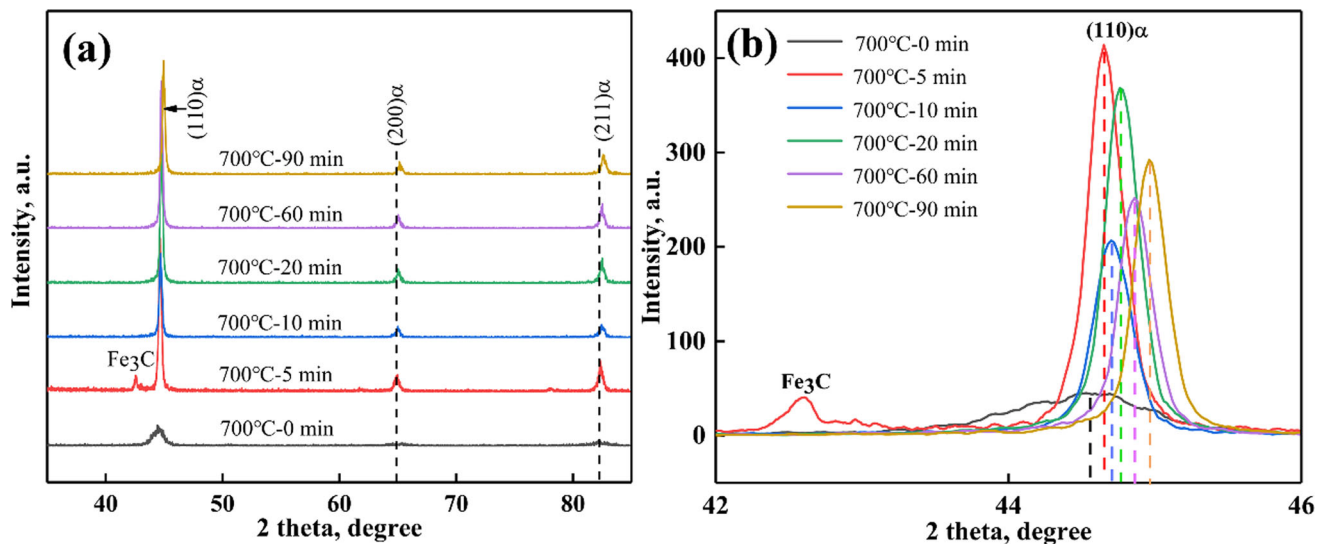


Fig. 4 (a) XRD patterns of the samples annealed at 700 °C for different time and (b) the corresponding magnified XRD patterns of (110)  $\alpha$  diffraction peaks

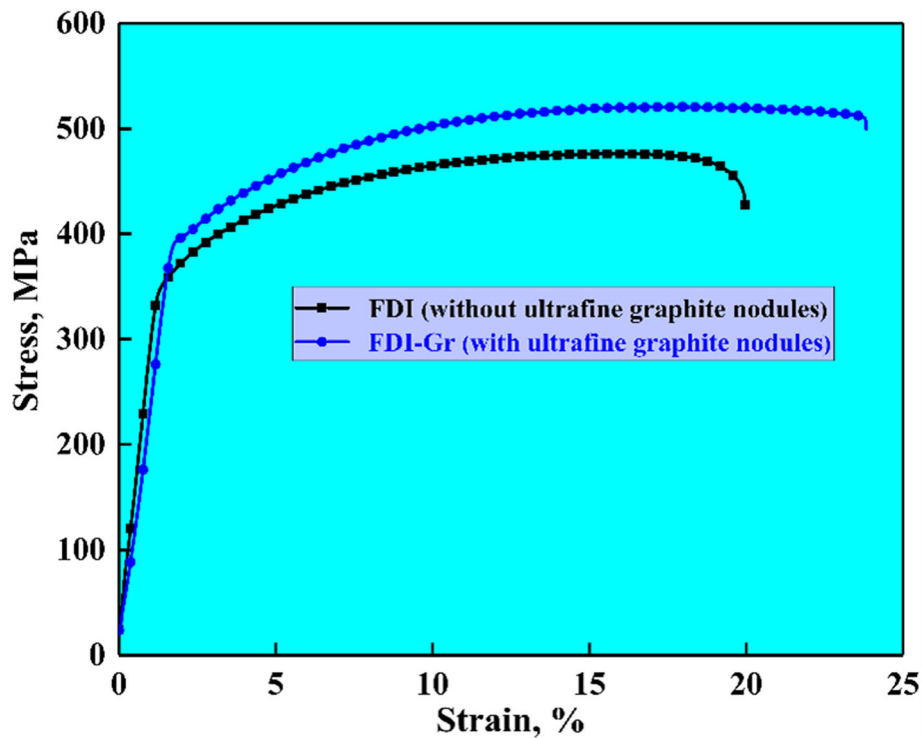


Fig. 5 Typical stress–strain curves of ductile iron having ferrite matrix with and without ultrafine graphite nodules

### 3.2 Effects of Graphite Precipitation on the Mechanical Properties of Ductile Iron

Figure 5 presents the typical stress–strain curves of ductile iron having ferrite matrix with and without ultrafine graphite nodule. The two samples were labeled as FDI-Gr and FDI, respectively, in the present study. It could be seen that the precipitation of ultrafine graphite nodule not only improved the strength but also enhanced the plasticity. FDI-Gr exhibited a yield strength of  $398 \pm 4$  MPa, an ultimate tensile strength of  $523 \pm 8$  MPa and an elongation of  $24.1 \pm 0.4\%$ . However, FDI only possessed the yield strength and ultimate tensile strength of  $364 \pm 2$  and  $473 \pm 6$  MPa the elongation of  $19.8 \pm 0.2\%$ .

## 4. Discussion

The microstructure showed that the ultrafine graphite nodules could be introduced in ductile iron with martensitic matrix by annealing treatment, which simultaneously improved the strength and plasticity of ferritic ductile iron.

### 4.1 Precipitation Mechanism of Ultrafine Graphite Nodule in Ductile Iron

Figure 6 shows the SEM images of the samples annealed for different times and corresponding EDS spectrum. Martensite was firstly decomposed into granular cementite and ferrite, and then, some ultrafine graphite nodules formed on ferrite (Fig. 6a). The phase A mainly contained iron atoms and a small amount of carbon atoms (Fig. 6A), indicating that A might be cementite. However, B contained about 70 at.% carbon atoms, which was far higher than the atomic fraction in

$\text{Fe}_3\text{C}$ . This indicated that the cementite was undergoing graphitization (Fig. 6B). C exhibited a few carbon atoms and the rest were iron atoms, which indicated the white small particles were residual cementite (Fig. 6b and C). It could be observed that ultrafine graphite nodules were formed on the ferrite matrix after annealing 90 min (Fig.6c). Pure graphite phase was observed in D (Fig. 6D).

Figure 7 illustrates the schematic diagram of precipitation process of the ultrafine graphite nodules in ductile iron during annealing. The precipitation of ultrafine graphite nodules from martensite contained the following four stages: martensitic decomposition, carbide aggregation and growth, graphitization of granular cementite and ultrafine graphite nodules formation. The as-cast ductile iron was composed of ferrite and pearlite (Fig. 7a). During austenitizing, ferrite and pearlite transform into austenite and carbon atoms of graphite diffuses toward austenite until the dissolved carbon atoms in graphite and austenite reach equilibrium state. Therefore, it is known that no less than 1.2% carbon atoms are dissolved in the austenitic matrix in ductile iron (Ref 37). Consequently, high carbon martensite with the acicular morphology was obtained after quenching treatment (Fig. 7b and c). During annealing, carbon atoms came out from supersaturated solid solution and form transitional  $\epsilon$ -carbide or cementite precipitates in martensite (Ref 38, 39). Carbides precipitated in a very short time during annealing because of the high carbon contents in martensite (Ref 26, 40). In the following annealing treatment, fine carbide particles gathered (Ref 41) and formed larger particles (Fig. 7d and e). With the extension of annealing time, the cementite would decompose and the carbon atoms would like to move toward the initial spheroidal graphite or form new graphite in the region far away from initial spheroidal graphite from the point view of thermodynamics. However, as a result, fine graphite nodules form far away from the initial spheroidal

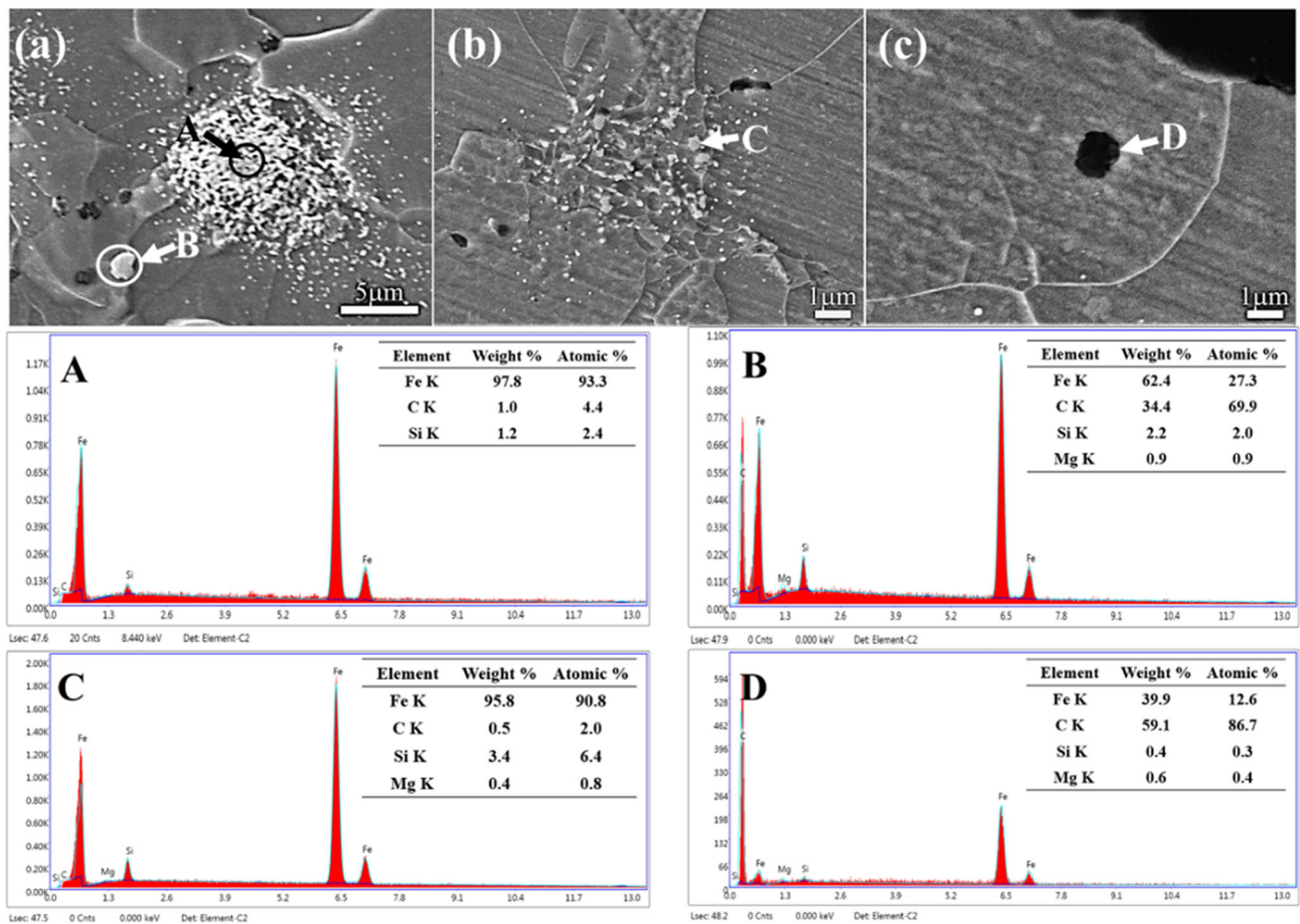


**Fig. 6** SEM images for annealing in martensite region: (a) 20 min, (b) 60 min and (c) 90 min; A, B, C and D are EDS spectrum collected from the corresponding areas

graphite. Additionally, the fine graphite nodules formed on the surface of initial spheroidal graphite integrate with the initial spheroidal graphite, which led to a rough surface of the initial spheroidal graphite after annealing (Fig. 7f).

#### 4.2 Effect of Ultrafine Graphite Nodule on Mechanical Properties

It has been indicated that the ductile iron with tiny graphite (FDI-Gr) exhibited a superior mechanical property compared with the ferritic ductile iron (FDI). Figure 8 shows the optical images of FDI and FDI-Gr. Although the two samples had ferrite matrix, the grain size of ferrite was different. The size of ferrite was about  $37 \pm 2.3$  and  $19 \pm 1.6 \mu\text{m}$  for FDI and FDI-Gr, respectively. The results indicated that the formation ultrafine graphite nodule in ductile iron after graphitizing annealing at  $700^\circ\text{C}$  for 90 min hindered the movement of ferrite boundary resulting in the formation of small ferritic grains, which should also be responsible for the enhanced mechanical properties of ductile iron after graphitizing annealing at  $700^\circ\text{C}$  for 90 min. The strength of graphite could be ignored compared ferrite matrix. Therefore, the FDI-Gr containing a fine ferrite exhibited a higher yield strength due to fine grain strengthening.

It should be noted that the interface of graphite/matrix is critical factor affecting the formation of cracks. Figure 9 illustrates the SEM images of deep-etched FDI and FDI-Gr

samples. It could be seen that the spheroidal graphite with relatively smooth surface could be observed for FDI, but FDI-Gr exhibited a very coarse surface. This was mainly because the migration of carbon atoms toward the spheroidal graphite during annealing treatment caused the formation of ultrafine graphite on the surface of initial spheroidal graphite. The fine graphite nodules were aggregated and tended to attach to the initial spheroidal graphite giving rise to a rough surface of initial spheroidal graphite for FDI-Gr. The rough surface of spheroidal graphite would reduce the bonds of graphite/matrix and induce the crack formation during deformation, which was harmful to the plasticity. However, the formation of ultrafine graphite nodule directly affects the stress distribution during tensile tests and thus the early cracking formation (Ref 42, 43). High graphite nodules were beneficial to the homogeneous distribution of stress. Compared with FDI, FDI-Gr had more graphite nodules but larger size difference. In order to analyze the effects of graphite on mechanical properties, the stress distribution in the two samples was simulated by 2D FE-model based on the microstructure in Fig. 8, given in Fig. 10. In the simulation process, spheroidal graphite was temporarily considered as voids. It could be seen that high stress preferred to distribute in the vicinity of the initial spheroidal graphite for the two samples. The stress near the ultrafine graphite nodule was very small. The stress distribution in FDI was more inhomogeneous than that of FDI-Gr (Fig. 10a and b), thus crack was easily initiated in FDI. Additionally, the ultrafine graphite

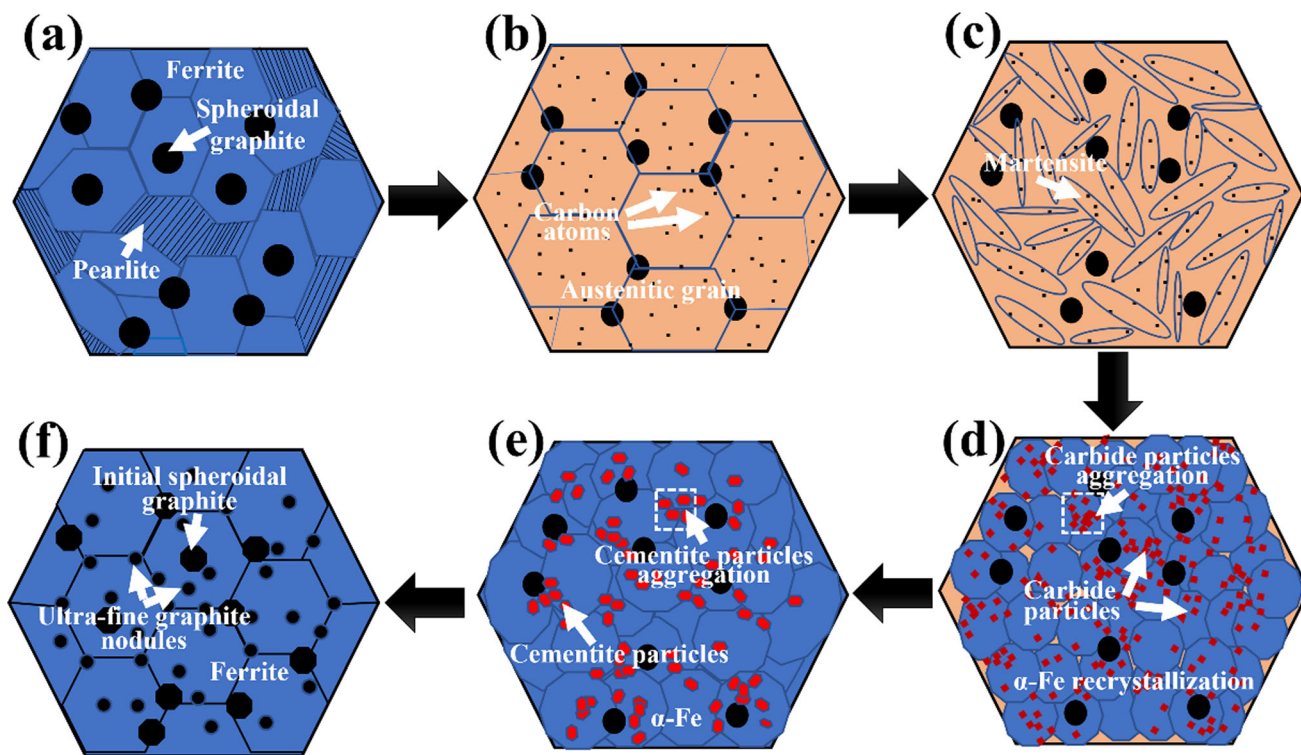


**Fig. 7** Schematic diagram of the precipitation process of the ultrafine graphite nodules in ductile iron during annealing: (a) the as-cast, (b) ductile iron with high temperature austenite matrix, (c) the quenched ductile iron, (d) carbon atoms precipitates from the martensite forming carbide, (e) carbide aggregated and (f) carbide decomposed into tiny graphite

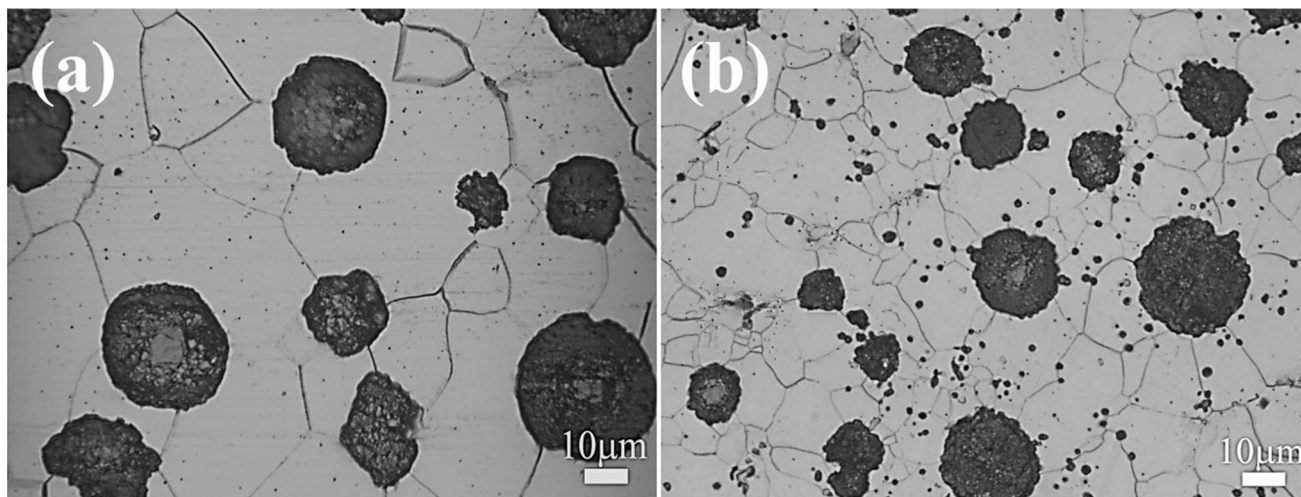


**Fig. 8** Optical images of ductile iron: (a) FDI and (b) FDI-Gr

nodule distributed between the initial large spheroidal graphite could hindered the propagation of cracks (Fig. 10b). Therefore, the precipitation of ultrafine graphite nodules in ductile iron benefited for the improvement of plasticity.

Figure 11 presents the typical fracture morphology of FDI and FDI-Gr after tensile tests. Dimples could be clearly observed for two samples (Fig. 11c and d), indicating plastic fracture. During the tensile testing, as plastic deformation increased, the interface between the large spheroidal graphite and the matrix debonding occurred, and tearing ridges were ultimately formed between the large spheroidal graphite,

indicating the occurrence of ductile fracture (Fig. 11c). However, it could be seen that a small degree of debonding occurred at the interface between the spheroidal graphite and the matrix. The interface between the ultrafine graphite nodule and the matrix mainly undergone debonding, which resulted in the formation of large number of small dimples around the small ultrafine graphite nodule (Fig. 11d). These small dimples would aggregate and merge during fracture, requiring more deformation energy. Thus, FDI-Gr exhibited a higher plasticity compared with FDI.

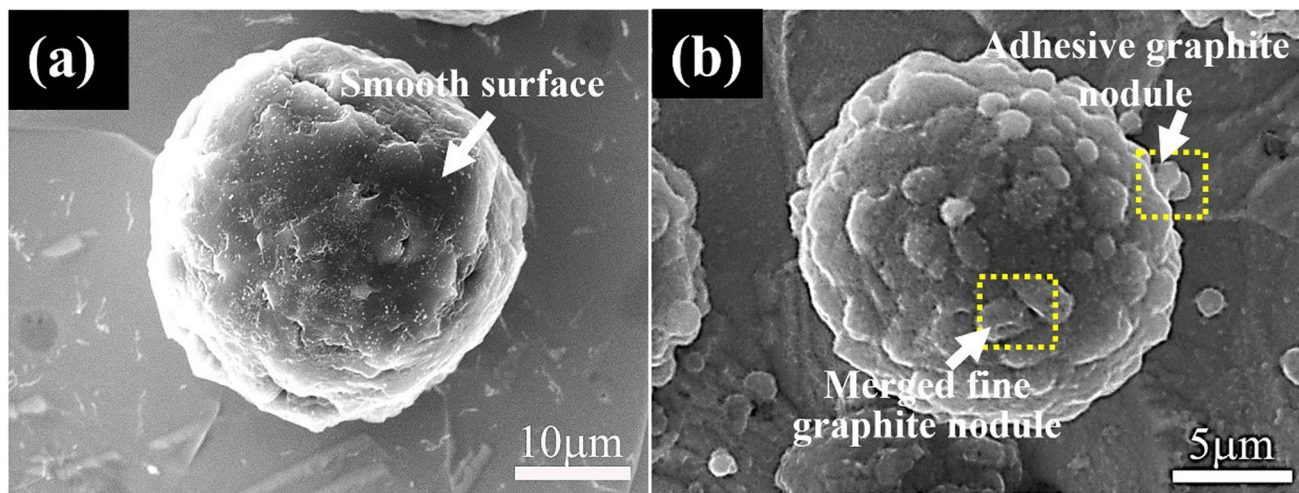


Fig. 9 SEM images of deep etched microstructure of spheroidal graphite in (a) FDI and (b) FDI-Gr

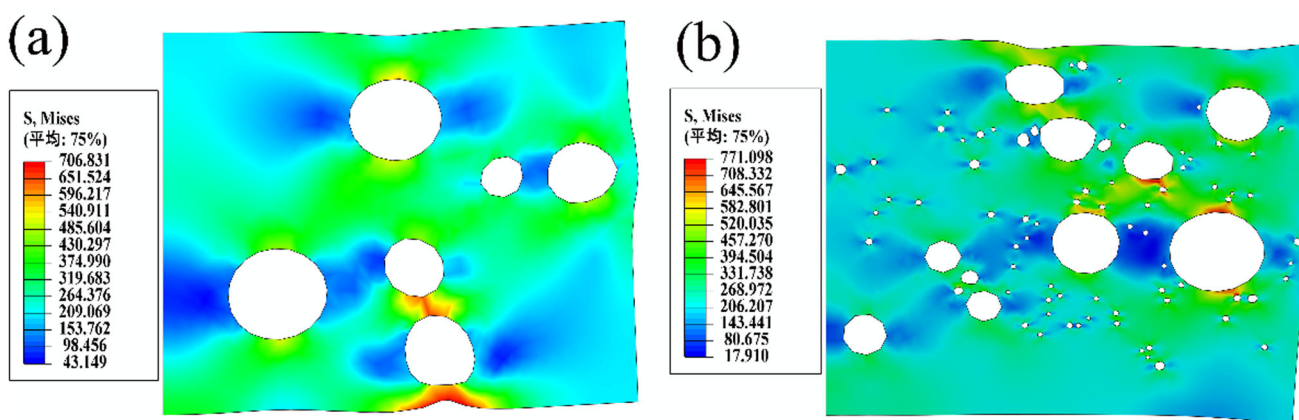


Fig. 10 Results of simulating stress distribution in the matrix based on Fig. 8: (a) FDI and (b) FDI-Gr

## 5. Implications for Further Modification of Graphite Nodules in Ductile Iron

The present study indicated that ultrafine graphite nodule could be obtained by heat treatment in ductile iron. Martensite as the starting microstructure in ductile iron was conducive to produce high graphite nodules count for ductile iron. A high austenitizing temperature and long austenitizing time could increase the solid solubility of carbon atoms in austenitic matrix; then, the ultra-high carbon martensite could be formed in the subsequent quenching process, which provided a new method to produce ductile iron with high graphite nodule count. The annealing time for obtaining the ultrafine graphite nodule was no more than 2 h, which was much shorter than that for white cast iron (5-8 h) (Ref 24). Additionally, the content of Si also played an important role in the formation of ultrafine graphite, which could inhibit the formation of carbides and promote their decomposition to form the graphite (Ref 44). For example, the formation of graphite usually required to specially add more than 1.8% Si in steels (Ref 26, 27). Coincidentally, the composition of ductile iron usually containing a large amount of Si (> 2%) was produced. Therefore, the ductile iron exhibited great advantages to form high graphite nodules count by solid phase transformation.

## 6. Conclusions

The microstructure evolution of ductile iron with martensite matrix was investigated during annealing treatment in the present study. The following conclusions could be drawn.

- (1) The ultrafine graphite nodules with a count of 8500 nod/mm<sup>2</sup> and an average diameter of 1 μm were produced in ductile iron with the starting microstructure of martensite via annealing treatment.
- (2) The martensite was first decomposed into granular cementite, and the aggregated granular cementite gradually transformed into ultrafine graphite nodules.
- (3) The ductile iron with the precipitated ultrafine graphite nodules exhibited a superior combination of strength and plasticity compared with ferritic ductile iron, which was because ultrafine graphite nodule refined ferrite grains, weakened stress concentration and hindered crack propagation during deformation.
- (4) This study provided a new approach to enhance graphite nodule counts in ductile iron through solid phase transformation.



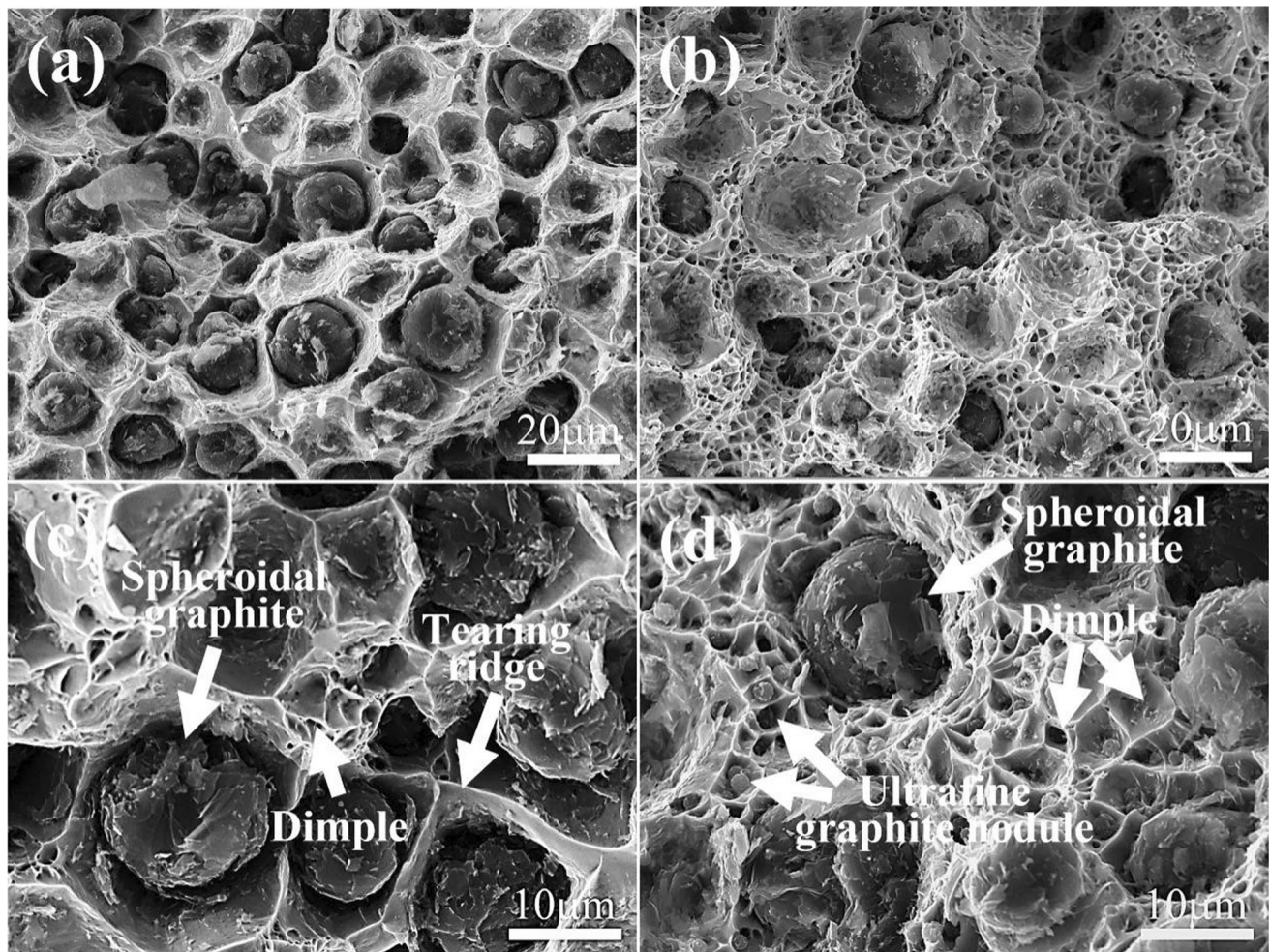


Fig. 11 SEM images of fracture morphology: (a, c) FDI and (b, d) FDI-Gr

### Acknowledgment

This work was supported by Shaanxi Natural Science Basic Research Program (No. 2023-JC-YB-293).

### Conflict of interest

The authors declare that they have no known competing financial interests or personal relationships that could have appeared to influence the work reported in this paper.

### References

1. D.M. Stefanescu, A History of Cast Iron, *Cast Iron Science and Technology*. ASM International, Detroit, 2017
2. A. Velichko, A. Wiegmann, and F. Mücklich, Estimation of the Effective Conductivities of Complex Cast Iron Microstructures Using FIB-Tomographic Analysis, *Acta Mater.*, 2009, **57**(17), p 5023–5035.
3. M. Benedetti, V. Fontanari, and D. Lusuardi, Effect of Graphite Morphology on the Fatigue and Fracture Resistance of Ferritic Ductile Cast Iron, *Eng. Fract. Mech.*, 2019, **206**, p 427–441.
4. D.M. Stefanescu, G. Alonso, P. Larrañaga, E. De la Fuente, and R. Suarez, Reexamination of Crystal Growth Theory of Graphite in Iron-Carbon Alloys, *Acta Mater.*, 2017, **139**, p 109–121.
5. Y. Liu, Y. Li, J. Xing, S. Wang, B. Zheng, D. Tao, and W. Li, Effect of Graphite Morphology on the Tensile Strength and Thermal Conductivity of Cast Iron, *Mater. Charact.*, 2018, **144**, p 155–165.
6. U. Tewary, D. Paul, H.K. Mehtani, S. Bhagavath, A. Alankar, G. Mohapatra, S.S. Sahay, A.S. Panwar, S. Karagadde, and I. Samajdar, The Origin of Graphite Morphology in Cast Iron, *Acta Mater.*, 2022, **226**, p 117660.
7. E. Ghassemali, J.C. Hernando, D.M. Stefanescu, A. Dioszegi, A.E.W. Jarfors, J. Dluhoš, and M. Petrevec, Revisiting the Graphite Nodule in Ductile Iron, *Scr. Mater.*, 2019, **161**, p 66–69.
8. J. Zhang, N. Zhang, M. Zhang, D. Zeng, Q. Song, and L. Lu, Rolling-Sliding Wear of Austempered Ductile Iron with Different Strength Grades, *Wear*, 2014, **318**(1), p 62–67.
9. R. Nan, H. Fu, P. Yang, J. Lin, and X. Guo, Microstructure Evolution and Wear Resistance of Cu-Bearing Carbide Austempered Ductile Iron after Austempering, *J. Mater. Eng. Perform.*, 2020, **29**(4), p 2440–2459.
10. B. Wang, G.C. Barber, C. Tao, X. Han, and X. Sun, Tribological Performance of Austempered and Tempered Ductile Iron, *Metall. Mater. Trans. B*, 2018, **49**(5), p 2261–2269.
11. H. Wang, Y. Feng, W. Jiang, C. Wang, E. Guo, Y. Fu, and S. Zhao, Effect of Niobium on Microstructure and Mechanical Properties of Ductile Iron with High Strength and Ductility, *J. Mater. Eng. Perform.*, 2023, **688**, p 416–428.
12. C. Liu, Y. Du, T. Ying, L. Zhang, X. Zhang, X. Wang, G. Yan, and B. Jiang, Effects of Graphite Nodule Count on Mechanical Properties and Thermal Conductivity of Ductile Iron, *Mater. Today Commun.*, 2022, **31**, p 103522.
13. X.L. Wang, Y.Z. Du, X.Q. Gao, Y.F. Ge, and B.L. Jiang, Influence of Graphite Nodules on the Microstructure and Mechanical Properties of Hollow Ductile-Iron Pipe After Austempering Treatment, *Steel Res. Int.*, 2019, **90**(12), p 1–7.

14. Z. Hu, X. Wang, Y. Du, C. Liu, Z. Gao, J. Li, and B. Jiang, Effects of Graphite Nodule Count on Microstructural Homogeneity of Austempered Ductile Iron (ADI), *Metall. Res. Technol.*, 2023, **120**(2), p 217–225.
15. R. Salazar F, M. Herrera-Trejo, M. Castro, J. Méndez N, J. Torres T, and M. Méndez N, Effect of Nodule Count and Cooling rate on As-cast Matrix of a Cu-Mo Spheroidal Graphite, *J. Mater. Eng. Perform.*, 1999, **8**(3), p 325–329.
16. L. Beltran-Sanchez, R. Ruxanda, J. Massone, and D.M. Stefanescu, On the Eutectic Solidification of Spheroidal Graphite Iron—an Experimental and Mathematical Modelling Approach, *Proc. Cast Iron Div. AFS Trans.*, 2001, **109**, p 1037–1047.
17. H. Itofuji, K. Edane, T. Kotani, M. Itamura, and A. Koichi, Ultrafine Spheroidal Graphite Iron Castings, *Metall. Trans.*, 2019, **60**(1), p 41–48.
18. Y.J. Kim and S.H. Park, Effect of Initial Microstructure on Graphitization Behavior of Fe-0.55C-2.3Si Steel, *J. Mater. Res. Technol.*, 2021, **15**, p 4529–4540.
19. A. Inam, R. Brydson, and D.V. Edmonds, Effect of Starting Microstructure Upon the Nucleation Sites and Distribution of Graphite Particles during a Graphitising Anneal of an Experimental Medium-Carbon Machining Steel, *Mater. Charact.*, 2015, **106**, p 86–92.
20. X.J. Gao, Q. Zhang, D.B. Wei, S.H. Jiao, and Z.Y. Jiang, Effects of Thermal and Thermomechanical Treatments on Sliding Wear of Graphite Crystallised White Cast Iron, *Wear*, 2013, **301**(1–2), p 656–662.
21. S. Aso, S. Goto, Y. Komatsu, and W. Hartono, Sliding Wear of Graphite Crystallized Chromium White Cast Iron, *Wear*, 2001, **250**(1), p 511–517.
22. J.Y. Park, K. Taek Choi, J.A. Szpunar, K. Hwan Oh, and H. Yong Ra, Effect of Mn Negative Segregation through the Thickness Direction on Graphitization Characteristics of Strip-Cast White Cast Iron, *Scr. Mater.*, 2002, **46**(3), p 199–203.
23. J. Wan, D.C. Van Aken, J. Qing, T.J. Yaniak, T.E. Clements, and M. Xu, Developing a Graphitic White Iron for Abrasive Wear Application: Thermal and Wear Properties, *Wear*, 2019, **436–437**, p 202967.
24. C. James, On the Annealing of White Cast Iron, *J. Franklin Inst.*, 1900, **150**(3), p 227–235.
25. Y.J. Kim, S.W. Bae, N.S. Lim, and S.H. Park, Graphitization Behavior of Medium-Carbon High-Silicon Steel and its Dependence on Temperature and Grain Size, *Mater. Sci. Eng. A*, 2020, **78**, p 1–7.
26. J.X. Gao, B.Q. Wei, D.D. Li, and K. He, Nucleation and Growth Characteristics of Graphite Spheroids in Bainite during Graphitization Annealing of a Medium Carbon Steel, *Mater. Charact.*, 2016, **118**, p 1–8.
27. A. Inam, R. Brydson, and D.V. Edmonds, A High-Resolution Study of Graphite Nodule Formation in Experimental Medium-Carbon Machining Steel, *Mater. Charact.*, 2017, **131**, p 508–516.
28. K. He, H.R. Daniels, A. Brown, R. Brydson, and D.V. Edmonds, An Electron Microscopic Study of Spheroidal Graphite Nodules Formed in a Medium-Carbon Steel by Annealing, *Acta Mater.*, 2007, **55**(9), p 2919–2927.
29. G. Alonso, D.M. Stefanescu, R. Gonzalez, and R. Suarez, Effect of Magnesium on the Solid-State Nucleation and Growth of Graphite during Annealing of White Iron, *Int. J. Metalcast.*, 2020, **14**(3), p 728–735.
30. R. Takahashi, Kinetics of Graphitization of White Cast Iron, *MRS Online Proc. Libr.*, 1984, **34**(1), p 305–313.
31. A. Inam, R. Brydson, and D.V. Edmonds, Raman Spectroscopy Study of the Crystallinity of Graphite Formed in an Experimental Free-Machining Steel, *Mater. Charact.*, 2020, **163**, p 110264.
32. A. Alhoussein, M. Risbet, A. Bastien, J.P. Chobaut, D. Balloy, and J. Favegeon, Influence of Silicon and Addition Elements on the Mechanical Behavior of Ferritic Ductile Cast Iron, *Mater. Sci. Eng. A*, 2014, **605**, p 222–228.
33. L.C. Chang, Carbon Content of Austenite in Austempered Ductile Iron, *Scr. Mater.*, 1998, **39**(1), p 35–38.
34. Y. Wang, Y. Zhang, R. Song, L. Huang, and Y. Pei, Effect of the Austenitizing Temperature on Microstructure Evolution and Impact Toughness of a Novel Bainite Ductile Iron, *Met. Mater. Int.*, 2020, **27**, p 4014–4020.
35. C.J. Xu, X.F. Xu, Z. Zhao, M. Ma, Z.M. Zhang, and Y.H. Liu, Horizontal Continuous Casting Technology of Cast Iron and Application of Dense Bars, *Foundry Technol.*, 2017, **38**(11), p 2559–2564.
36. J. Zhang, Z. Dai, L. Zeng, X. Zuo, J. Wan, Y. Rong, N. Chen, J. Lu, and H. Chen, Revealing Carbide Precipitation Effects and Their Mechanisms during Quenching-Partitioning-Tempering of a High Carbon Steel: Experiments and Modeling, *Acta Mater.*, 2021, **217**, p 117176.
37. A.S. Nishikawa, G. Miyamoto, T. Furuhashi, A.P. Tschiptschin, and H. Goldenstein, Phase Transformation Mechanisms during a Ductile Cast Iron, *Acta Mater.*, 2019, **179**, p 1–16.
38. L. Morsdorf, E. Emelina, B. Gault, M. Herbig, and C.C. Tasan, Carbon Redistribution in Quenched and Tempered Lath Martensite, *Acta Mater.*, 2021, **205**, p 116521.
39. D.V. Edmonds, K. He, F.C. Rizzo, B.C. De Cooman, D.K. Matlock, and J.G. Speer, Quenching and Partitioning Martensite-A Novel Steel Heat Treatment, *Mater. Sci. Eng. A*, 2006, **438–440**, p 25–34.
40. L. Morsdorf, A. Kashiwar, C. Kübel, and C.C. Tasan, Carbon Segregation and Cementite Precipitation at Grain Boundaries in Quenched and Tempered Lath Martensite, *Mater. Sci. Eng. A*, 2023, **862**, p 144369.
41. S. Li, M. He, G. Hu, Y. Tian, C. Wang, B. Jing, and D. Ping, Pearlite Formation via Martensite, *Compos. B Eng.*, 2022, **238**, p 109859.
42. Y. Tanaka, Z.L. Yang, and K. Miyamoto, Evaluation of Fatigue Limit of Spheroidal Graphite Cast Iron, *Metall. Trans.*, 1995, **36**(6), p 749–756.
43. A.C. Melado, A.S. Nishikawa, H. Goldenstein, M.A. Giles, and P.A.S. Reed, Effect of Microstructure on Fatigue Behaviour of Advanced High Strength Ductile Cast Iron Produced by Quenching and Partitioning Process, *Int. J. Fatigue*, 2017, **104**, p 397–407.
44. S.Y. Lu, T.F. Chung, J.J. Chen, Y.W. Lai, C.N. Hsiao, C.Y. Chen, S.H. Wang, and J.R. Yang, Development of Microstructures-Properties in Fe-0.4C/0.2C-2Si-3Mn Carbide-Free Bainite Steels, *Mater. Charact.*, 2023, **197**, p 112670.

**Publisher's Note** Springer Nature remains neutral with regard to jurisdictional claims in published maps and institutional affiliations.

Springer Nature or its licensor (e.g. a society or other partner) holds exclusive rights to this article under a publishing agreement with the author(s) or other rightsholder(s); author self-archiving of the accepted manuscript version of this article is solely governed by the terms of such publishing agreement and applicable law.